Atomic-Resolution Elemental Mapping by EELS and XEDS in Aberration Corrected STEM

M. Watanabe†, M. Kanno†† and E. Okunishi††

† **Department of Materials Science and Engineering / Center for Advanced Materials and Nanotechnology, Lehigh University**
†† **EM Business Unit, JEOL Ltd.**

Recent improvements in aberration correction have brought tremendous advantages not only in high resolution imaging but also in high resolution analysis by electron energy-loss spectrometry (EELS) and X-ray energy-dispersive spectrometry (XEDS) in scanning transmission electron microscopy (STEM). Once the incident probe formation is optimized, atomic-resolution analysis can be performed by acquiring sufficient enough signals for appropriate chemical analysis while maintaining fine probe sizes. In addition, more sophisticated approaches of data acquisition and analysis, such as spectrum imaging (SI) and multivariate statistical analysis (MSA), are essential for atomic-resolution chemical analysis. In fact, it is possible to obtain atomic-resolution chemical images of materials since both the spatial resolution and analytical sensitivity are improved tremendously in combination of the aberration correction instrument with the advanced acquisition and analysis techniques. In this manuscript, the incident probe formation, data acquisition and data analysis are reviewed for atomic-resolution chemical analysis by EELS and XEDS in aberration-corrected instruments. Then, several applications of atomic-resolution chemical images obtained by the recently developed JEM-ARM200F aberration-corrected microscope are shown to address future trends in chemical analysis of materials.

Introduction

Chemical analysis at atomic-level spatial resolution with single-atom detection sensitivity is one of the ultimate goals in materials characterization. Such atomic-level materials characterization is now possible in the latest aberration-corrected electron microscopes. By aberration correction, image resolution has already reached half-Ångstrom levels by high-angle annular dark-field (HAADF) imaging in scanning transmission electron microscopy (STEM) and phase contrast imaging in transmission electron microscopy (TEM) [1, 2]. In addition, aberration-corrected STEM is also useful for chemical analysis by electron energy-loss spectrometry (EELS) and X-ray energy dispersive spectrometry (XEDS) since more probe current can be added into the aberration-corrected fine probe. Especially for EELS analysis, such higher beam currents may be sufficient to generate core-loss signals for reasonable analysis within a short acquisition time. Atomic-resolution EELS mapping has been already demonstrated in aberration-corrected STEM [3-5]. The aberration-corrected fine probe is also beneficial for XEDS analysis to analyze materials with improved spatial resolution of ~0.4 nm [6].

Elemental mapping in aberration-corrected STEM/TEM is still limited by poor analytical sensitivity due to far much shorter acquisition time per pixel and to extremely small analyzed volumes. By simply increasing acquisition time, atomic-level resolution may be spoiled by spatial drifts of a specimen and/or an incident probe. Increased probe currents to improve analytical sensitivity result in degradation of resolution as the incident probe is enlarged with the current. Therefore, it is essential to optimize probe setting with an suitable probe currents for atomic resolution analysis. In addition, the poor analytical sensitivity can be offset by applying spectrum imaging (SI) in combination with advanced statistical approaches, such as multivariate statistical analysis (MSA). These methods succeed because the major noise components can be removed efficiently from spectrum acquired for a very short dwell time and then regular spectral processing is potentially applicable. The MSA noise reduction is also applicable to atomic resolution images as well.

In this paper, the optimum probe-formation is discussed first to perform atomic-resolution chemical analysis by EELS and XEDS in aberration-corrected instruments. Then, advantages to employ advanced SI and MSA approaches are demonstrated to extract unexpected information from datasets. Finally, several applications of atomic-resolution chemical images obtained by the recently developed JEM-ARM200F are shown to address future trends in chemical analysis of materials.

5 E. Packer Ave., Bethlehem, PA 18015, USA.

masashi.watanabe@lehigh.edu

Optimum instrument settings for atomic resolution analysis

Spatial resolution in STEM imaging and analysis is directly related to an incident probe dimension; i.e., the shape and diameter in a certain fraction Hence, the incident probe dimension is one of the most important factors in STEM. Most of the probe formation discussed in previous studies are focused on the geometric-aberration limited probe (dealt with a point source) and/or chromatic-aberration limited probe (which represent blurring of a point source). Note that the details about the geometric- and chromatic-aberration limited probe-formation can be found in the literature [e.g. 7-9]. Neither geometric- nor chromatic-aberration limited probe dimension contains any contribution of the finite source size (which is expressed through the source brightness and probe current). Therefore, the geometric- or chromatic-aberration limited probe sizes are useful only for operating conditions with a significantly limited probe current [10], such as high resolution HAADF-STEM imaging. However, for any analytical application by EELS and XEDS, the contribution of the finite source must be taken into account to probe formation since more currents are required to generate sufficient enough signals for appropriate EELS or XEDS analysis [6, 11]. In fact, the probe dimensions are enlarged as a function of the probe current.

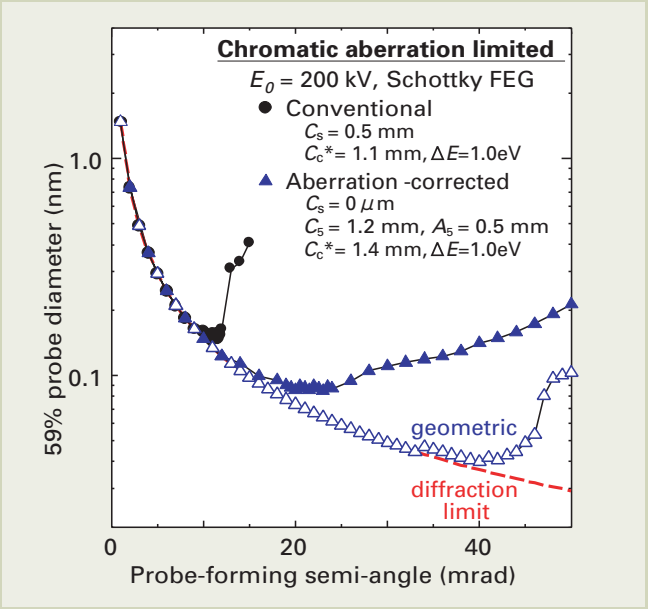

Fig. 1 Chromatic-aberration limited probe diameter contains 59% of the total intensity simulated for conventional and aberration-corrected 200 kV instrument with a Schottky FEG, plotted against the probe-forming semi-angle α. For comparison, the diffraction limit diameter and the geometric-aberration limited probe diameter in the aberration-corrected conditions are also plotted.

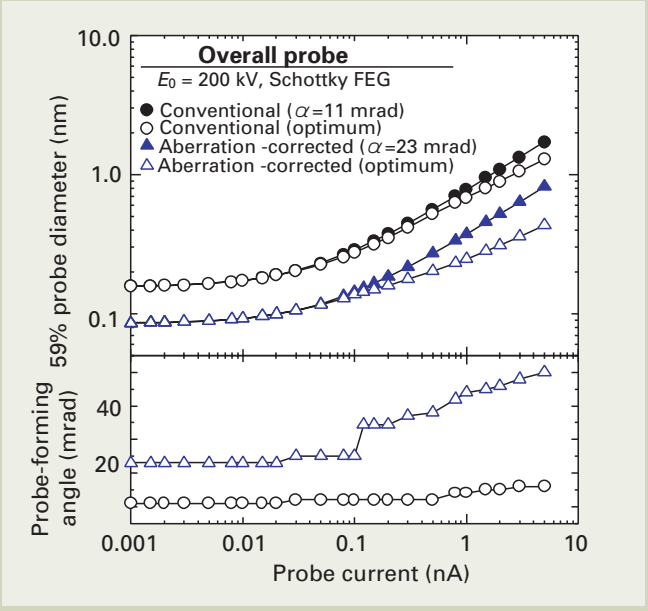

Fig. 2 Optimum angle for the overall probe in the conventional and aberration-corrected conditions summarized as a function of the probe current with the corresponding probe diameter d(59%) for the Schottky FEG [12].

Hence, probe setting should be optimized carefully to maintain the high spatial resolution in atomic level with sufficient probe currents for better analytical sensitivity. Here, the optimum probe setting for atomic resolution analysis is discussed first [12].

Figure 1 shows the diameter containing 59% of total intensity d(59%), determined from the simulated intensity distribution of chromatic-aberration limited probe in conventional and aberration-corrected conditions for a 200 kV JEOL instrument equipped with a Schottky field-emission gun (FEG) source, which are plotted as a function of the probe-forming semi-angle, α. In the both conditions, the electron energy-spread (ΔE) of 1.0 eV that is a common value for the Schottky FEG was used. Note that the definition of d(59%) is originally derived from the Rayleigh criterion of intensity distribution in the aperture-diffraction limited probe, by which the image resolution can be defined as the minimum distance to distinguish the two point objects [9, 13, 14]. In the conventional condition, the simulation was performed for a 200 kV JEOL instrument with a ultra-high resolution pole-piece (the 3rd-order spherical aberration coefficient C_s of 0.5 mm and the chromatic aberration coefficient C_c* of 1.1 mm). Even though these aberration coefficients are the best value available in commercial instruments without an aberration corrector, the major limit is the 3rd-order spherical aberration and the probe diameter can be at best 160 pm at α = 11 mrad with a defocus of –28 nm. In contrast, the residual aberrations can be the 5th-order spherical aberration (C_5) and six-fold astigmatism (A_5) after complete aberration tuning in a CEOS hexapole-based corrector system [15, 16]. With the residual aberrations of C_5 = 0.5 mm and A_5 = 1.2 mm, the geometric-aberration limited probe size can reach to 40 pm at ~40 mrad as shown in Fig. 1 (open triangle). In the aberration-corrected condition, however, the major limitation can be the chromatic aberration and the optimum angle is reduced only to 23 mrad. Then, the optimum probe size is degraded to 85 pm from 40 pm due to the chromatic aberration. In this case, the probe diameter was determined with ΔE = 1.0 eV and C_c* = 1.4 mm (slightly increased due to the addition of aberration corrector).

As shown in Fig. 1, the optimum probe sizes are 160 pm at 11 mrad and 85 pm at 23 mrad in the conventional and aberration-corrected conditions, respectively. Again, these probe sizes are based on the chromatic-aberration limited intensity distribution and any contribution of the finite source size is not included. For analytical applications, the probe optimization should be performed with the probe current. The overall probe diameters at 11 and 23 mrad in both conventional and aberration-corrected conditions (closed symbols) are plotted against the probe current in **Fig. 2**. The probe size is enlarged with an increase of the probe current in both conditions. In addition, the optimum overall diameters (open symbols) are also plotted in Fig. 2, which is calculated by determination of the optimum probe-forming angle. The optimum angle in the conventional condition is slightly increased with an increase of the current. Conversely, much larger probe-forming angle can be employed in the aberration-corrected condition especially when the probe current is higher than 100 pA, which is essential for EELS and XEDS analysis. Further details

about the probe optimization can be found elsewhere [12, 17].

Figure 3 shows simulated intensity distributions and extracted line profiles of the overall probes at probe currents of (a) 30, (b) 120 and (c) 500 pA in an aberration-corrected 200 kV instrument with a Schottky source. These selected probe currents are typical values for HAADF-STEM imaging, EELS analysis and XEDS analysis, respectively. The simulation was performed at optimum convergence angles for corresponding probe currents, as shown in Fig. 2. Both the intensity distributions and the profiles are normalized with the peak intensity at 500 pA. Therefore, the peak intensities at lower current conditions are correspondingly lower (i.e., ~57% at 30 pA and ~70% at 120 pA against the peak intensity at 500 pA). In the profiles, the normalized chromatic-aberration limited profiles are also plotted as dashed lines. At 30 pA, the dominant contribution is chromatic/geometric aberrations to the final probe formation. However, at higher currents for analysis applications, finite source size is the dominant factor for probe formation. Simulated d(59%) values at 30, 120 and 500 nA are 118, 152 and 220 pm, respectively.

Figure 4 shows HAADF-STEM images of Si<110> recorded at (a) 30, (b) 120 and (c) 500 pA in an aberration-corrected 200 kV JEOL JEM-2200FS STEM with a Schottky FEG at Lehigh. Intensity profiles extracted from the individual images are also inserted in Fig. 3. At 30 pA, the intensity reduction between the atomic column of the Si dumbbell reaches over 25%, which satisfies the Rayleigh criterion as described previously. The intensity reduction is slightly degraded at 120 pA, and no reduction can be observed at 500 pA. These experimental results are superimposed with the simulated d(59%) values as shown in Fig. 3.

For atomic-resolution chemical analysis, the probe optimization is the crucial factor. In addition, spatial resolution caused by the convolution of the incident probe with probe broadening must be maintained in atomic level. Since the beam broadening is strongly dependent on the specimen thickness, the spatial resolution should be evaluated as a function of the specimen thickness. In addition, since analytical signals of X-ray and energy-loss electrons are generated from the whole analyzed volume, it would be more appropriate to employ 90% of the total intensity rather than 59% for evaluation of the spatial resolution. In the evaluation, therefore, the selected incident probe diameters of 1.2 and 0.4 nm for the conventional and aberration-corrected cases, respectively, (which correspond to the d(90%) values in optimum probe-forming conditions at a current of 500 pA) are used. **Figure 5** shows the spatial resolution (90%) calculated for a Cu thin specimen in the conventional and aberration-corrected conditions at 200 kV based on the Gaussian probe broadening model [18-20], plotted against the specimen thickness. Obviously, a finer probe size in the aberration-corrected condition provides better spatial resolution. In the aberration-corrected condition, the spatial resolution remains below 1 nm for specimen thicknesses up to ~30 nm in pure Cu. More importantly, the spatial resolution can reach atomic dimensions below thicknesses of 20 nm. Conversely, thicker specimen > 50 nm in Cu ends up with similar spatial resolution in both the conditions, which implies that there is no significant benefit to use an aberration-corrected STEM for improved spatial resolution if a thicker specimen is analyzed. For atomic resolution analysis, therefore, thinner specimens are essential. It should be noted that electron channeling was not taken into account for evaluation of spatial resolution. If a crystalline thin specimen is oriented near a highly symmetric zone axis, the incident probe-specimen interaction can be localized near a single atomic-column or surrounding neighbor columns due to the electron channeling, which may result in better spatial resolution rather than simple evaluation based on the Gaussian beam-broadening.

Advanced data acquisition and analysis procedures

As predicted above, thinner specimens are essential for atomic-resolution chemical analysis. This means that the analyzed volume is extremely restricted, and hence generated signals for appropriate analysis are also limited. In addition, signal fluctuations are not completely predictable in atomic resolution analysis as shown later. Therefore, advanced approaches for data acquisition and analysis are essential to detect such signal fluctuations from limited signals under relatively high noise in atomic resolution analysis.

Spectrum imaging (SI) has been developed to expand and improve conventional elemental mapping [21, 22], which requires prior knowledge of the specimen to set particular energy windows. In SI, a full spectrum is continuously recorded at each pixel. Thus, the SI method offers post-acquisition treatments of elemental maps including regular spectral-processing methods, such as background subtraction and signal deconvolution. Therefore, it is possible to map out unexpected minor elements that are not even considered for mapping beforehand if the signals from such minor elements are successfully identified. However, for characterization of elemental fluctuations in atomic resolution, elemental mapping including SI in STEM still suffers from limited signals. Furthermore, there might be many variables even in a single SI dataset: some could be expected and others are totally unaware. It is essential to find out those variables in the dataset, which can be performed by employing multivariate statistical analysis (MSA).

The MSA method is a useful family of statistic-based techniques to analyze large datasets. The general concept of MSA is to reduce the dimensionality of an original large dataset by finding a minimum number of variables that describe the original dataset without losing any significant information [e.g., 23, 24]. This approach is useful for large, complicated data such as XEDS or EELS SI datasets,

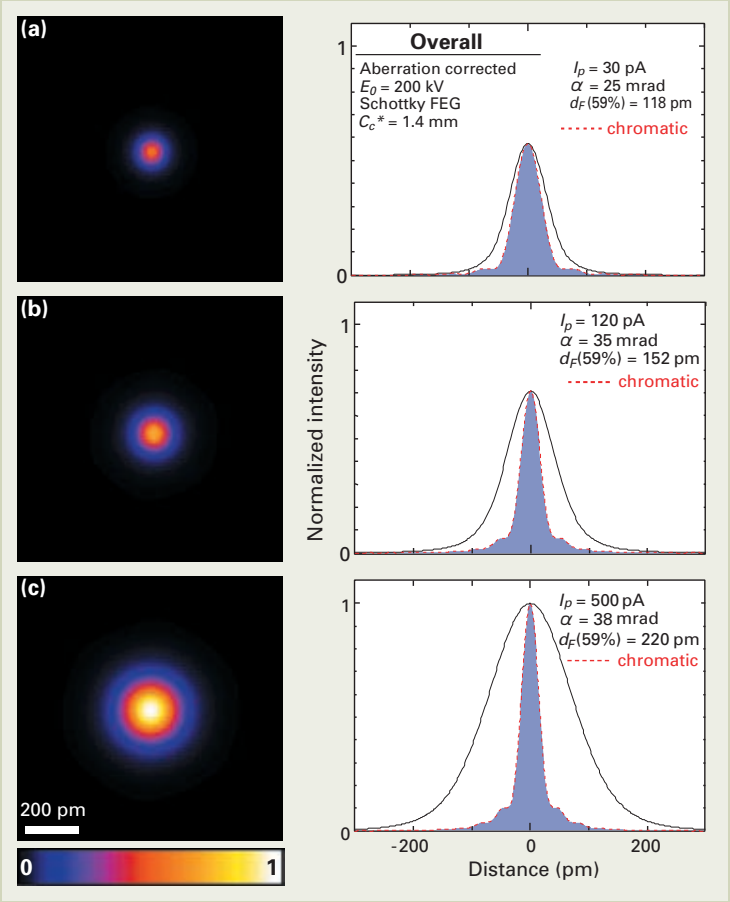

Fig. 3 Simulated intensity distributions and extracted line profiles of the overall probes at the probe currents of (a) 30, (b) 120 and (c) 500 pA in an aberration-corrected 200 kV instrument with a Schottky FEG. Normalized chromatic-aberration limited intensity profiles simulated at corresponding probe-formation conditions are also plotted as dashed lines in the profiles [17].

which has been successfully demonstrated by Koluta et al. [25].

For example, a STEM-EELS SI dataset was taken from $SrTiO_3$ in an aberration-corrected JEM-2200FS instrument at 200 kV. A HAADF-STEM image from a $SrTiO_3$ thin specimen is shown in **Fig. 6**(a) [26]. The bright and slightly darker spots in the image correspond to the Sr and Ti-O columns in the [001]-projected perovskite structure, respectively, and an EELS-SI data was acquired from the region indicated as a dashed square with 13×13 pixels for a dwell time of 0.1 s per pixel. Two spectra at the Sr and Ti-O column positions extracted from the SI are compared in Fig. 6 (b). Although the spatial difference spectrum (Fig.6c) between the spectra from the Sr and Ti-O columns shows a reduction in the vicinity of the Sr $M_{2,3}$ edge and an enhancement in the Ti $L_{2,3}$ edge, both spectra seem almost identical and it would be harder to distinguish one spectra from another. To confirm the difference in the spectra between the Sr and Ti-O columns, MSA was applied to the dataset. By applying the MSA method, the SI dataset can be decomposed to loading and score matrices: the former contains spectral feature uncorrelated to other row information and the later represents the spatial amplitude of the corresponding loading spectrum. In **Fig. 7**, pairs of the loading spectrum and the corresponding score image of the (a) first and (b) second components are compared. The most significant component in the dataset is always the average (i.e., the average information is repeated at every pixel), and hence the loading spectrum of the first component represents the average spectrum of the SI dataset. Sr $M_{2,3}$ and Ti $L_{2,3}$ edges can be seen in this SI dataset. Any component after the first component indicates the difference from the average. Therefore, loading spectra after the first component contain positive and negative regions. The brighter regions in the score image of second component correspond to the Ti-O atom-

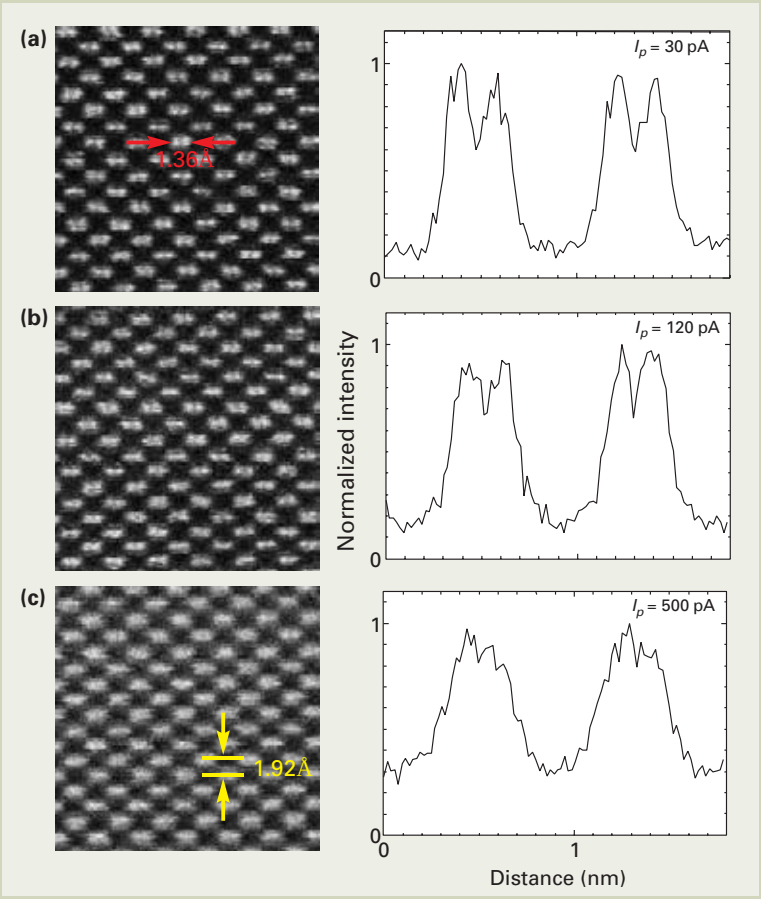

Fig. 4 HAADF-STEM images of [110]-projected Si recorded at (a) 30, (b) 120 and (c) 500 pA in an aberration-corrected 200 kV JEOL JEM-2200FS STEM with a Schottky FEG. Normalized intensity profiles extracted from the individual images are also inserted for comparison [17].

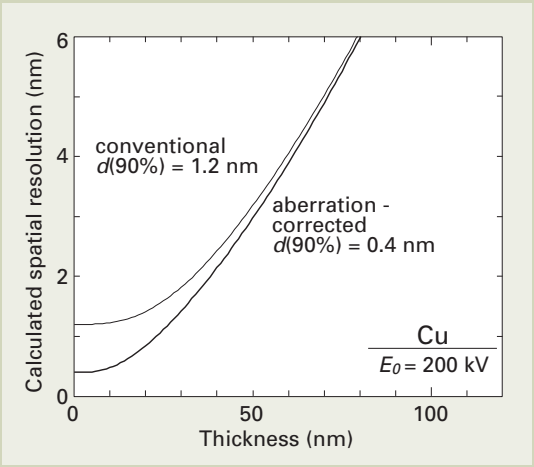

Fig. 5 Spatial resolution (90%) calculated for a Cu thin specimen in conventional and aberration-corrected conditions at 200 kV based on the Gaussian probe broadening model, as plotted against the specimen thickness [17].

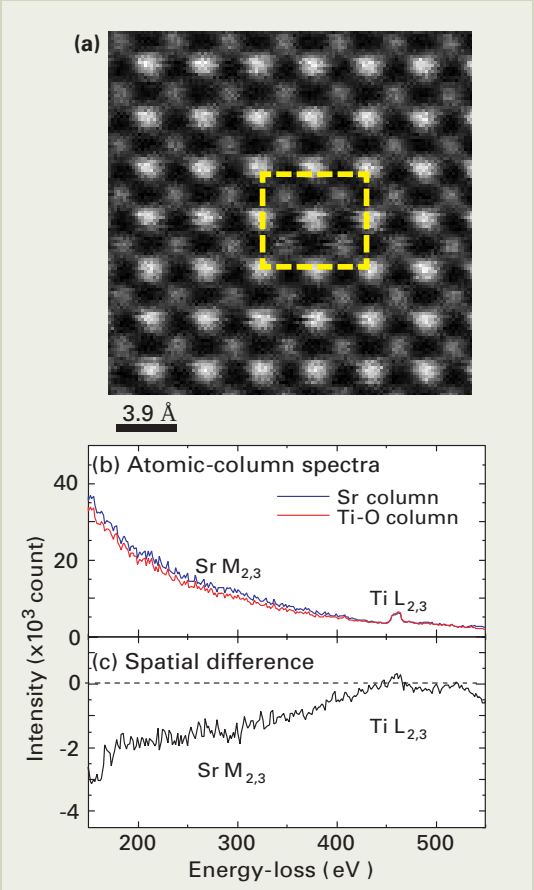

Fig. 6 (a) HAADF-STEM image of a [001]-projected $SrTiO_3$ specimen. From a region indicated as a dashed square, an EELS-SI data was acquired with 13×13 pixels for a dwell time of 0.1 s per pixel. (b) Two spectra at the Sr and Ti-O column positions extracted from the SI are compared. (c) The spatial differential spectrum [26].

ic-columns, where the Ti $L_{2,3}$ edge signal is more enhanced and the Sr $M_{2,3}$ edge signal is reduced. This second component agrees well with the spatial difference spectrum shown in Fig. 6(c), i.e. the Ti $L_{2,3}$ edge signals are clearly increased at the Ti-O columns in $SrTiO_3$. Therefore, the signal fluctuation in different atomic-columns is real and essentially one of the dominant features repeated a number of times in the dataset.

In addition, MSA may reveal unexpected features in the dataset as well. **Figure 8** shows another example of the MSA application to atomic-column EELS SI dataset taken from a [0001]-projected Si_3N_4 specimen by an aberration-corrected JEM-2010F STEM at 200 kV [27]. The SI dataset was recorded with 50×45 pixels and 670 energy-channels (with binning 2) using a Gatan Enfina spectrometer for a dwell time of 20 ms. The first two components extracted from the dataset by MSA are shown in Fig. 8. Again, the average is the most frequently repeated information in the dataset (component #1) as shown in Fig. 8a. In the component #2 (Fig. 8b), the brighter regions in the score image correspond to the Si atom positions in the six-fold ring. Surprisingly, this enhancement at Si atom positions occurs not at the Si $L_{2,3}$ edge, but after the Si L_1 edge as shown in the spectrum of component #2. This resolution difference in a different energy-loss region can be due to the delocalization-effect dependence on the offset energy from the ionization edge, as recently discussed by Kimoto et al. [28]. Such unique correlations of spectral features with specific spatial locations might not be identified accurately unless these correlations are well known prior to data acquisition/analysis. However, by applying MSA, these unexpected features can be automatically revealed, based on numbers that the features are repeated.

After dominant features are identified in the dataset, the original dataset can be described with a limited number of the featured components, and then random noise that is not repeated at all can be efficiently removed from the dataset. The data reconstruction without random noise components results in the enhancement of weak signals in SI datasets. In the SI dataset from atomic-resolution Si_3N_4, the noise reduction was applied by subtracting noise components. **Figure 9** compares Si $L_{2,3}$ edge (a) and Si L_1 edge (b) maps extracted with background subtraction from the original and MSA-reconstructed datasets. This comparison of maps from the original and reconstructed datasets clearly demonstrates the efficient removal of the noise. The reconstructed maps from both the Si $L_{2,3}$ and L_1 edges maps show Si atom arrangement with a six-fold ring. The Si atom arrangement in the six-fold ring is more clearly pronounced in the Si L_1 map, and the individual Si atomic columns can be clearly distinguished, as expected from component #2 shown in Fig. 8(b).

Recently, one of the authors (MW) has developed the MSA software package as a series of plug-in for Gatan DigitalMicrograph Suite [29]. This particular MSA plug-in package has been applied for various SI datasets acquired by EELS and XEDS [3, 5, 29-32]. This package is now available through HREM Research Inc. Further information can also be found at the company's web site [33] or the author's web site [34].

Applications of atomic-resolution chemical mapping in the JEM-ARM200F

STEM-EELS based chemical imaging

For atomic-level analysis, the STEM probe must be positioned above individual atomic column sites during acquisition, which requires relatively long-term instrumental and environmental stabilities. Two examples of atomic-resolution EELS imaging shown above were taken from the 1st generation JEOL aberration-corrected STEMs, which were constructed by adding the CEOS correctors to existing microscope columns. The newly developed JEOL JEM-ARM200F aberration-corrected STEM instrument is designed to perform the atomic-level chemical analysis with improved instru-

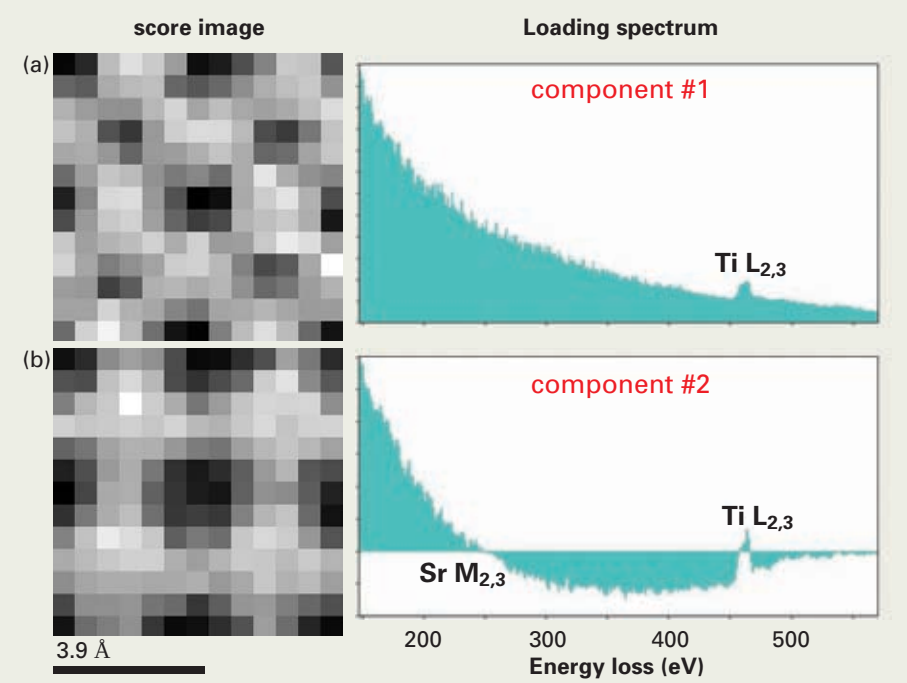

Fig. 7 Pairs of loading spectrum and corresponding score image of component #1 (a) and #2 (b) of an atomic-resolution STEM-EELS SI dataset from $SrTiO_3$ [26].

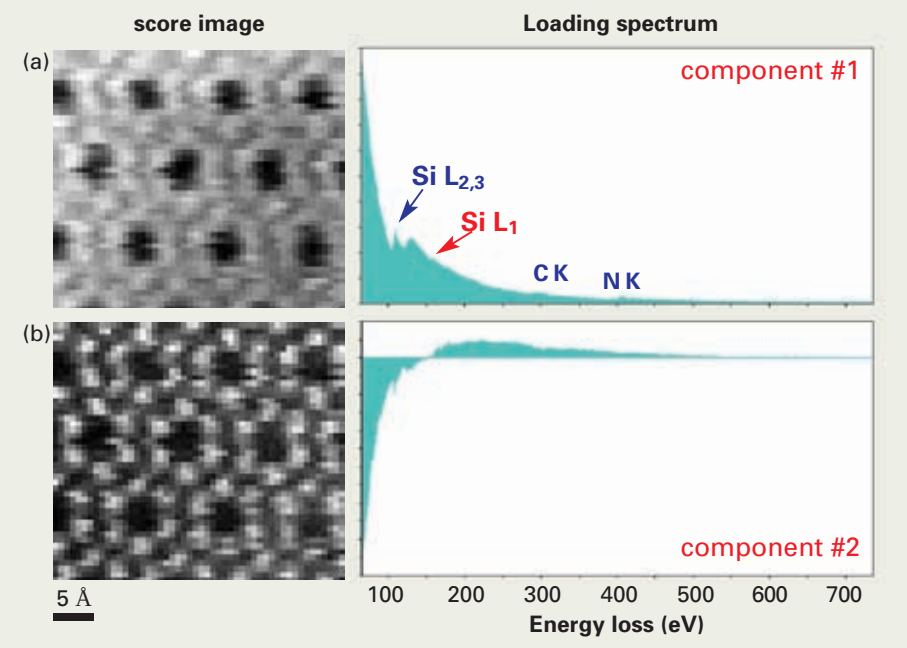

Fig. 8 Pairs of loading spectrum and corresponding score image of component #1 (a) and #2 (b) of an atomic-resolution STEM-EELS SI dataset from Si_3N_4 [27].

mental stabilities. Some of the major improvements of the JEM-ARM200F are: (i) significantly reduced mechanical instabilities by optimizing the column stiffness to accommodate the probe corrector; (ii) efficient suppression of external influences, such as stray electro-magnetic fields, temperature/pressure fluctuations, air flows and sound vibrations, by the incorporation of a heat insulation shield, a magnetic shield and an external mechanical cover; and (iii) reductions in instabilities of the accelerating voltage, objective/condenser lens currents and deflector coils by a factor of 2 from the first generation instruments[35]. The spatial drift rate in the new instrument is 0.5 nm/min.

The improved performance for atomic-resolution analysis in the newly developed JEM-ARM200F is shown in **Fig. 10**, as an example. An HAADF-STEM image from an interface in a $LaMnO_3/SrTiO_3$ multilayer thin-film is shown in Fig. 10(a). The bright and slightly fainter spots appearing in this HAADF-STEM image correspond to heavy atomic columns of La or Sr and to Ti-O or Mn-O columns in the perovskite structure, respectively. An EELS SI data was acquired from the same field of view with 186×26 pixels and 1350 channels for a dwell time of 0.1 s using a Gatan Enfina spectrometer. After applying MSA, elemental maps were extracted by power-low background subtraction. From the extracted elemental maps, two RGB color-overlay images were constructed as shown in Fig. 10(b, Red: Ti $L_{2,3}$, Green:

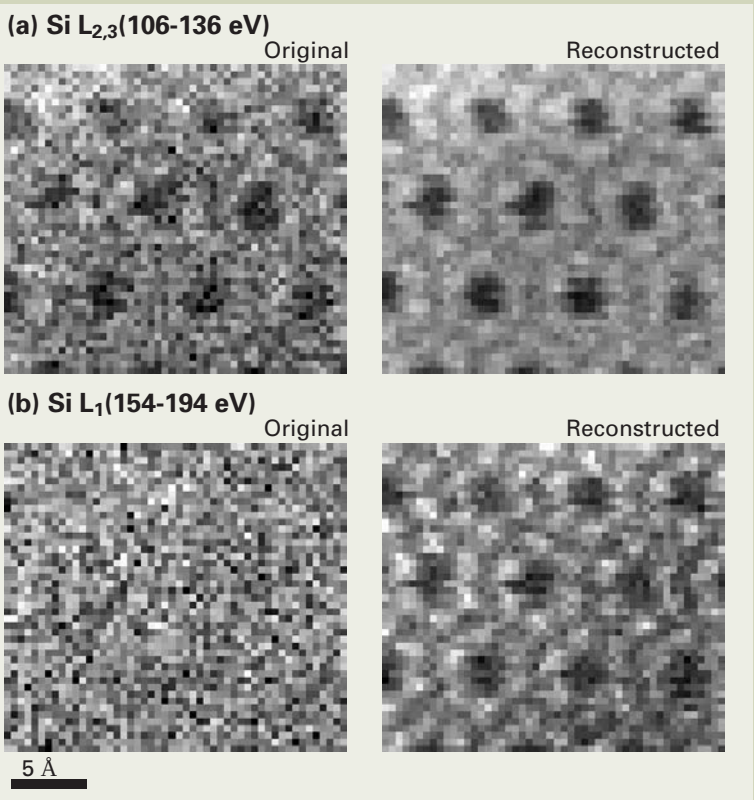

Fig. 9 Comparison of characteristic signal maps of (a) Si $L_{2,3}$ and (b) Si L_1 edges extracted from the original and MSA-reconstructed SI datasets of Si_3N_4 with background subtraction [27].

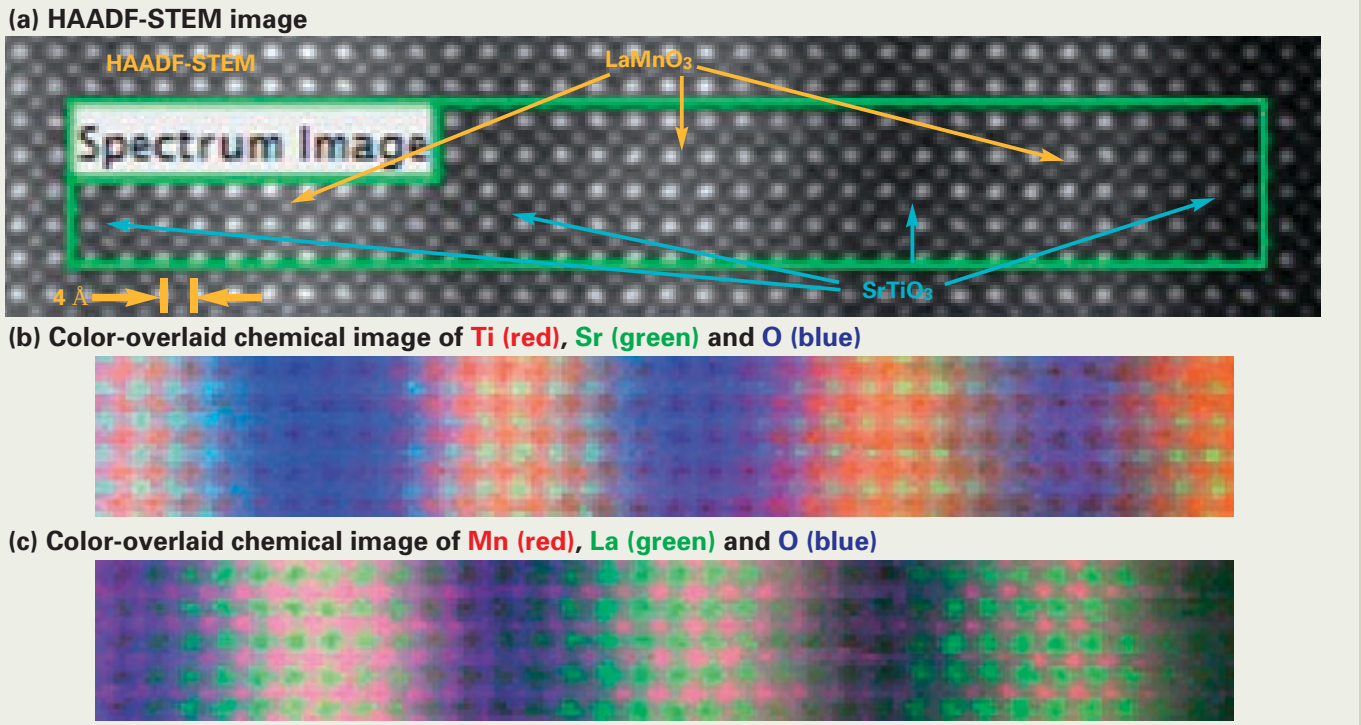

Fig. 10 (a) HAADF-STEM image from a $LaMnO_3/SrTiO_3$ interface, (b) RGB color-overlay image of $SrTiO_3$ and (c) RGB color-overlay image of $LaMnO_3$, obtained by the EELS approach (Specimen courtesy of Drs. Maria Varela and Ho Nyung Lee at Oak Ridge National Lab.) [36].

Sr $M_{2,3}$ and Blue: O K) and 1(c, Red: Mn $L_{2,3}$, Green: La $M_{4,5}$ and Blue: O K), which represent $SrTiO_3$ and $LaMnO_3$ layers, respectively [36]. Elemental distributions can be obtained from much larger fields of view, which is only possible in the improved stability in the JEM-ARM200F. In addition, at individual atomic columns can be clearly distinguished. Especially the Ti distribution is terminated at the $LaMnO_3/SrTiO_3$ interfaces relatively sharply, whereas the Mn distribution seems diffused toward $SrTiO_3$ layers.

STEM-XEDS-based Chemical Imaging

As shown above, atomic-resolution EELS imaging is routinely applicable in aberration-corrected STEM with better resolution and improved stability [e.g., 3-5]. For X-ray analysis, such atomic-column analysis or even atomic-column mapping has not even been attempted, mainly because atomic-resolution STEM images are not obtainable with the higher probe currents (and consequent large probes) required for X-ray analysis in conventional STEM instruments due to poorer signal collection efficiency as discussed above (~100 times worse than EELS). However, since the aberration correction makes it possible to reduce the incident probe size while maintaining higher currents, it may be feasible to perform atomic-column X-ray analysis. In fact, the spatial resolution of X-ray analysis is improved to ~0.4 nm [6] and the detectability limit may approach a few atoms [17], which implies atomic-level analysis/mapping by X-ray analysis is feasible in aberration-corrected STEM.

Using the JEM-ARM200F microscope, GaAs was analyzed at an atomic scale by the XEDS approach [36]. **Figure 11** (a) shows an atomic-resolution HAADF-STEM image of [001]-projected GaAs. In this projection, the Ga and As layers are separated, as shown schematicaly in Fig. 11 (b) (drawn by Vesta [37]). Since the difference in the atomic number is only two between Ga (31) and As (33), the Z-contrast between two elements may not appear unless a very thin specimen is observed. An XEDS SI dataset was recorded from the squared area shown in Fig. 11 (a), and then MSA was performed to improve weak signals in the dataset. In Fig. 11 (c), the second component extracted by MSA is shown as a pair comprising the loading spectrum and the score image. The loading spectrum shows positive K and L peaks of Ga and negative K and L peaks of As. Therefore, the brighter regions in the score image must correspond to the Ga columns, whereas the darker regions correspond to the As columns. Thus, this particular component definitely shows the signal separation between Ga and As. **Figure 12** shows a HAADF-STEM image (a) and X-ray maps of Ga Kα and As Kα lines with their color overlay image (b), X-ray maps of Ga L and As L lines with their color overlay image (c), and EELS maps of Ga $L_{2,3}$ and As $L_{2,3}$ edges with their color overlay image (c), which were also simultaneously recorded with the XEDS SI dataset. Although the signal levels are still very limited in comparison with EELS results, atomic-level XEDS analysis is now possible through the combination of aberration-corrected STEM and MSA. If the detection efficiency of X-ray signals is improved, atomic-column X-ray mapping would be routinely applicable.

Summary

In this manuscript, the optimum probe-formation in aberration-corrected STEMs was reviewed for atomic-resolution chemical analysis by EELS and XEDS. The new approaches for data acquisition by SI and for data analysis via MSA were discussed as well. By applying MSA, unexpected information hidden in a SI dataset can be revealed. In addition, random noise in the datasets can be efficiently reduced by MSA. This combination of SI with MSA is very useful for analysis of atomic-column datasets, where unexpected signal correlations might be hidden over relatively high random noise due to the short acquisition time and the small analytical volume, as shown in several examples. It is now possible to perform atomic-resolution chemical imaging by STEM-EELS and STEM-XEDS methods in the latest aberration-corrected instrument, such as the JEM-ARM200F. In near future, the atomic-resolution chemical imaging approach would be routinely available for materials characterization.

Acknowledgements

One of the authors (MW) wishes to acknowledge the support of the National Science Foundation through grant (DMR-0804528). The authors would also like to thank Prof. David Williams (currently at the Univ. of Alabama, Huntsville) for his thoughtful supervision for many years. In addition, the author would like to thank Prof. Christopher Kiely and Mr. David Ackland at Lehigh for long-term collaboration, Dr. Kazuo Ishizuka and Mr. Kenta Yoshimura at HREM Research Inc. for development of the MSA plugin, Dr. Hidetaka Sawada at JEOL ltd. for discussion in probe simulation, and Dr. Maria Varela and Dr. Ho Nyung Lee at Oak Ridge National Lab. for providing the $LaMnO_3/SrTiO_3$ multilayer specimen.

References

[1] R. Erni, at al., *Phys. Rev. Lett.*, **102**, 096101 (2009).
[2] H. Sawada, et al., *J. Electron Microsc.*, **58**,

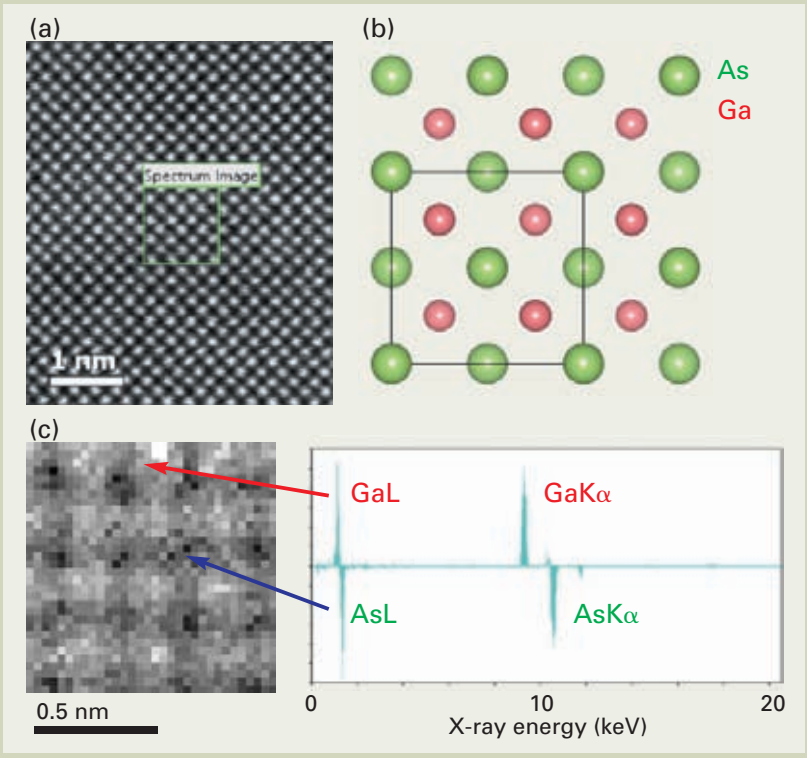

Fig. 11 (a) HAADF-STEM image taken from a [001]-projected GaAs specimen. An X-ray SI dataset was acquired from the selected squared region in the aberration-corrected JEM-ARM200F; (b) a schematic diagram of arrangements of Ga and As atoms in the [001]-projected GaAs, as drawn by Vesta [39]. (c) a pair of loading spectrum and score image of a statistically significant component extracted from the X-ray SI dataset by applying MSA [36].

357, (2009).
[3] M. Bosman, et al., *Phys. Rev. Lett.*, **99**, 086102 (2007).
[4] D.A. Muller, et al., *Science*, **319**, 1073 (2008).
[5] M. Varela, et al., *Phys. Rev. B*, **79**, 085117 (2009).
[6] M. Watanabe, et. al., *Microsc. Microanal.* **12**, 515 (2006).
[7] E. Munro, in Proc. *8th Int. Congr. on X-Ray Optics and Microanalysis* (ed. by R. Ogilvie and D. Wittry), paper no. 19. (NBS, Washington DC, 1977).
[8] C. Colliex, C. Mory, in *Quantitative Electron Microscopy*, ed. by J.N. Chapman, A. Craven, (Scottish University Summer School in Physics, Glasgow, Scotland, 1984), p. 149
[9] M. Haider, et al., *Ultramicroscopy* **81**, 163 (2000)
[10] J.E. Barth, P. Kruit, . *Optik* **101**, 101 (1996).
[11] L.M. Brown, *J.Phys. F: Metal Phys.* **11**, 1, (1981).
[12] M. Watanabe, H. Sawada, *Ultramicrosc.*, (submitted).
[13] J. Fertig, H. Rose, Optik, **54**, 165 (1979).
[14] H. Rose, *Nuclear Inst. Methods*, **187**, 187 (1981).
[15] H. Müller, et al., *Microsc. Microanal.*, **12**, 442 (2006).
[16] H. Sawada, et al., *J. Electron Microsc.*, **58**, 341 (2009).
[17] M. Watanabe, "X-ray Analysis in Aberration-Corrected Analytical Electron Microscopes" in *Scanning Transmission Electron Microscopy: Imaging and Analysis*, Eds. Stephen J. Pennycook and Peter D. Nellist (in print).
[18] P. Doig, et al., *Philos. Mag. A* **41**, 761 (1980).
[19] P. Doig, P.E.J. Flewitt, *Met. Trans. A* **13**, 1397 (1982)
[20] E. Van Cappellan, A. Schmitz, *Ultramicrosc.* **41**, 193 (1992).
[21] C. Jeanguillaume, C. Colliex, *Ultramicrosc.*, **28**, 252 (1989).
[22] J.A. Hunt, D.B. Williams, *Ultramicrosc.*, **38**, 47 (1991).
[23] I.T. Jolliffe, Principal component analysis. 2nd ed. Springer, New York, (2002).
[24] E.R. Malinowski, Factor analysis in chemistry. 3rd ed. Wiley, New York, (2002).
[25] P.G. Kotula, et al., *Microsc. Microanal.* **9**, 1 (2003).
[26] M. Watanabe, et al., *Microsc. Microanal.* 13 (2007), Suppl. 2, 1264.
[27] M. Watanabe, et al., *Microscopy and Analysis*, **23**, Issue 7, 5, (2009).
[28] K. Kimoto, et al., *Micron*, **39**, 257, (2008).
[29] M.G. Burke, et al., *J. Mater. Sci.* **41**, 4512, (2006).
[30] M. Bosman, et al., *Nanotechnology* **18** 165505 (2007).
[31] T. Yaguchi, et al., *Ultramicrosc.*, **108**, 1603, (2008).
[32] M. Bosman, et al., *Carbon*, **47**, 94, (2009).
[33] http://www.hremresearch.com/Eng/plug-in/MSAEng.html.
[34] http://www.lehigh.edu/~maw3/research/msamain.html.
[35] I. Ishikawa, et al., *Microsc. Microanal.*, **15**, Suppl. 2, 188 (2009).
[36] M. Watanabe, et al., *Microsc. Microanal.* **16** (2010),(in press).
[37] K. Momma, F. Izumi, *J. Appl. Crystallogr.*, **41**, 653 (2008).

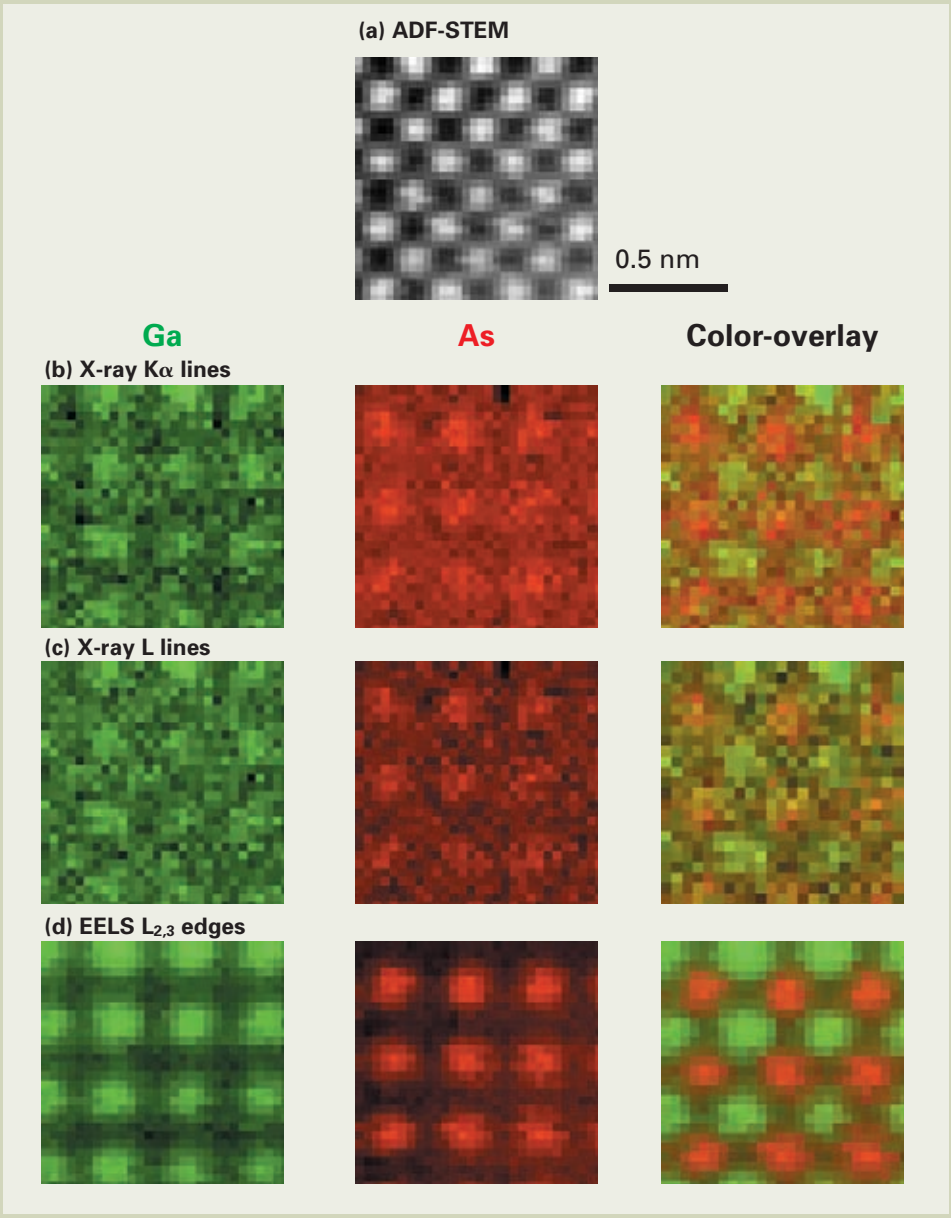

Fig. 12 (a) HAADF-STEM image of the [001]-projected GaAs simultaneously recorded during SI acquisition; a set of a Ga maps, an As map and a color-overlay map of Kα X-ray lines (b), L X-ray lines (c) and EELS $L_{2,3}$ edges (d) [36].